Magnetic Switching Dynamics and Tunnel Magnetoresistance Effect Based on Spin-Splitting Noncollinear Antiferromagnet Mn_3Pt

Meng Zhu(朱蒙)†, Jianting Dong(董建艇)†, Xinlu Li(李新录), Fanxing Zheng(郑凡星), Ye Zhou(周晔), Kun Wu(吴琨), and Jia Zhang(张佳)*

School of Physics and Wuhan National High Magnetic Field Center, Huazhong University of Science and Technology, Wuhan 430074, China

(Received 16 January 2024; accepted manuscript online 25 March 2024)

In comparison to ferromagnets, antiferromagnets are believed to have superior advantages for applications in next-generation magnetic storage devices, including fast spin dynamics, vanishing stray fields and robust against external magnetic field, etc. However, unlike ferromagnetic orders, which could be detected through tunneling magnetoresistance effect in magnetic tunnel junctions, the antiferromagnetic order (i.e., Néel vector) cannot be effectively detected by the similar mechanism due to the spin degeneracy of conventional antiferromagnets. Recently discovered spin-splitting noncollinear antiferromagnets, such as Mn_3Pt with momentum-dependent spin polarization due to their special magnetic space group, make it possible to achieve remarkable tunneling magnetoresistance effects in noncollinear antiferromagnetic tunnel junctions. Through first-principles calculations, we demonstrate that the tunneling magnetoresistance ratio can reach more than 800% in Mn_3Pt/perovskite oxides/Mn_3Pt antiferromagnetic tunnel junctions. We also reveal the switching dynamics of Mn_3Pt thin film under magnetic fields using atomistic spin dynamic simulation. Our study provides a reliable method for detecting Néel vector of noncollinear antiferromagnets through the tunnel magnetoresistance effect and may pave its way for potential applications in antiferromagnetic memory devices.

DOI: 10.1088/0256-307X/41/4/047502

Antiferromagnets (AFMs) have been promising candidates for the emerging field of magnetic information storage devices due to their excellent energy efficiency, terahertz spin dynamics, and absence of stray fields.[1,2] However, one of the major obstacles in this field is the lack of an effective electrical readout method of the antiferromagnetic order parameter, i.e., the Néel vector. In the past few years, significant strides have been taken to identify the Néel vector of AFMs through methods such as anisotropic magnetoresistance[3,4] and spin-Hall magnetoresistance effects.[5,6] Nevertheless, these approaches face practical limitations as the generated electric signals are typically very small, often less than 1%. In addition, the device dimensions are generally large, making these methods less suitable for practical applications.[7]

The standard electrical readout method for ferromagnetic states is via the so-called tunneling magnetoresistance (TMR) effect[8] in magnetic tunnel junctions (MTJs) such as CoFe/AlO_x/CoFe[9,10] and CoFeB/MgO/CoFeB,[11,12] where the junction resistance depends on the magnetic alignments of two ferromagnets. Ferromagnetic tunnel junctions, with large TMR ratios up to several hundred percent, have been widely used as the workhorse materials for various spintronic devices, including read head in a hard disk drive and storage cell in magnetic random-access memory.[13] Therefore, it would be desirable to have similarly substantial TMR effect in antiferromagnetic tunnel junctions (AFMTJs). Unfortunately, achieving significant TMR effects in AFMTJs faces feasibility challenges owing to the spin-degenerated band structures in most conventional AFMs such as MnPt, IrMn, Mn_2Au, and CuMnAs.[14,15] These challenges have, in turn, impeded the progress in developing antiferromagnetic memory devices.

Recently, according to theoretical predictions, AFMs belonging to specific magnetic space groups (MSGs) exhibit spin-splitting band structures even in the absence of spin-orbit coupling (SOC).[15,16] Since the spin-splitting AFMs carry momentum-dependent spin polarization, AFMTJs with AFM/Barrier/AFM structures may produce sizable TMR effects, which provides a reliable mechanism for detecting AFM Néel vectors. For instance, thanks to the split band of altermagnet RuO_2,[17,18] TMR around 100% has been predicted in RuO_2/barrier/RuO_2 AFMTJ. In addition, robust Hall effects[19] and longitudinal spin-conductivity[20] have also been predicted due to the magnetic structure of RuO_2. However, the Néel temperature of RuO_2 is around 300 K,[21] which is still not high enough for practical device applications. What's worse, it is difficult to manipulate the Néel vector of collinear AFMs by current or magnetic field.

Typical representatives of spin-splitting AFMs also in-

†Meng Zhu and Jianting Dong contributed equally to this work.

*Corresponding author. Email: jiazhang@hust.edu.cn

© 2024 Chinese Physical Society and IOP Publishing Ltd

clude noncollinear $D0_{19}$ hexagonal AFMs Mn_3X ($X = Sn$, Ge, Ga) and cubic Mn_3Pt, Mn_3Ir, and Mn_3Rh, etc. These noncollinear AFMs with Néel temperature well above 300 K are promising candidates for antiferromagnetic spintronic devices and have been found to exhibit fascinating spin-dependent transport properties, including anomalous Hall effect,[22,23] spin Hall effect,[24,25] and magnetic spin Hall effect.[26] Indeed, as demonstrated in previous work,[27] TMR high up to 120% has been predicted in Mn_3Sn/1T-HfO_2/Mn_3Sn AFMTJ. However, considering the fact that the lattice constant of hexagonal Mn_3Sn ($a = b = 5.665$ Å, $c = 4.531$ Å)[28] does not well match with generally used oxide tunnel barriers, it is difficult to experimentally fabricate single-crystalline AFMTJs based on Mn_3Sn. Moreover, the predicted TMR in Mn_3Sn-based AFMTJ is limited and still one order of magnitude smaller than that of conventional Fe/MgO/Fe MTJ.[11] Therefore, there is plenty of room for improving TMR in noncollinear AFMTJs through material and interface engineering.

The lattice constants of spin-splitting noncollinear AFMs in the cubic phase, such as Mn_3Pt, Mn_3Ir, and Mn_3Rh, closely align with those of perovskite oxides. Notably, studies indicate the successful growth of Mn_3Pt films on $BaTiO_3$ substrates, exhibiting tiny remanent magnetization.[29] Furthermore, it has been observed that the Néel vector of Mn_3Pt can be effectively manipulated by an external magnetic field, with a coercive field H_c measuring approximately 50 Oe.[30] Therefore, one may expect that single-crystalline Mn_3Pt/perovskite oxides/Mn_3Pt AFMTJs are experimentally achievable.

In this Letter, we first investigate the magnetic switching process of Mn_3Pt films with different thickness by using atomistic spin dynamic simulations. We then examine the features of momentum-dependent spin polarization of Mn_3Pt with noncollinear antiferromagnetic spin configurations under positive and negative 0.6 T magnetic fields. Finally, we build Mn_3Pt-based AFMTJs using perovskite oxides $PbTiO_3$ and $SrTiO_3$ as tunnel barriers, and investigate their quantum transport properties. Our calculation results indicate that the coercive fields H_c of Mn_3Pt films are linearly proportional to its thickness, which can be attributed to the change of magnetic moment directions of the three Mn atoms in Mn_3Pt as the film thickness increases. The TMR ratio high up to several hundreds of percent can be accessible in the proposed Mn_3Pt/perovskite/Mn_3Pt AFMTJs.

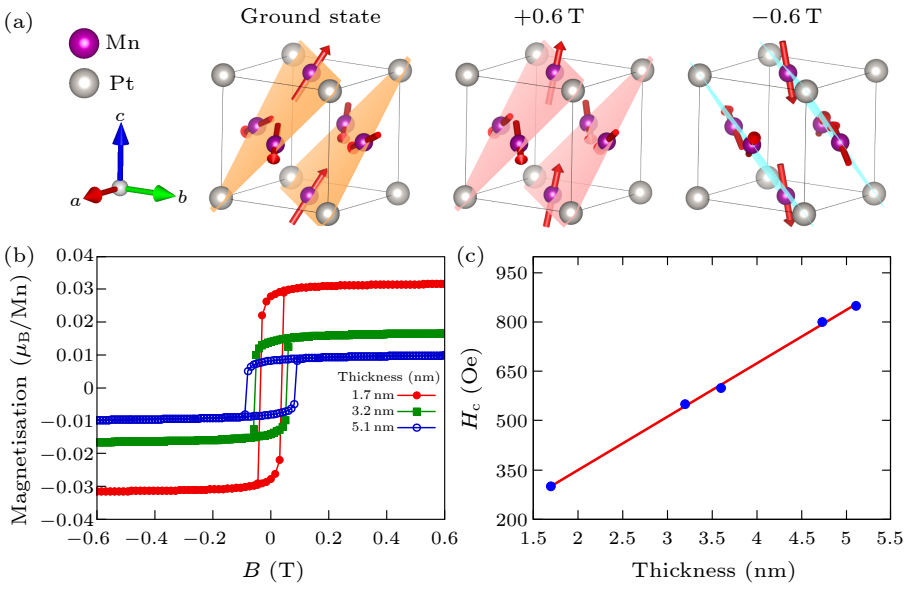

Fig. 1. (a) Crystal structure, simulated antiferromagnetic ground state, and spin configurations of Mn_3Pt (from left to right) under positive and negative 0.6 T magnetic field. (b) Simulated magnetic hysteresis loop, and (c) coercive field H_c of Mn_3Pt versus film thickness.

To gain an insightful understanding on the switching process of Mn_3Pt film under magnetic field, atomistic spin dynamics simulations have been conducted based on the Landau–Lifshitz–Gilbert (LLG) equation by using the VAMPIRE package.[31] The spin Hamiltonian of Mn_3Pt film has been modeled by considering interatomic exchange interaction and Néel pair anisotropy as follows:[32]

$$H = -\sum_{i<j} J_{ij}(\boldsymbol{S}_i \cdot \boldsymbol{S}_j) - \frac{k_N}{2}\sum_{i\neq j}^{z}(\boldsymbol{S}_i \cdot \boldsymbol{e}_{ij})^2,$$

where $\boldsymbol{S}_i$ is a unit vector representing the spin direction on site i, J_{ij} are the isotropic Heisenberg exchange interactions between neighboring pairs, k_N is the Néel pair constant, z is the number of nearest neighbors, $\boldsymbol{e}_{ij}$ is a unit vector pointing from site i to site j. In our simulations, the Néel pair constant k_N is set to -1×10^{-25} J, while the effective nearest and next-nearest Heisenberg exchange interactions are taken as $J_{ij}^{nn} = -4.19 \times 10^{-21}$ J, $J_{ij}^{nnn} = 2.15 \times 10^{-21}$ J. The selection of these magnetic interaction parameters aligns with experimentally observed key properties, including the antiferromagnetic ground state, Néel temperature and the coercive field of Mn_3Pt

films. For example, as illustrated in Fig. 1(a), the antiferromagnetic ground state of Mn_3Pt calculated under zero magnetic field, manifests as a triangular noncollinear spin structure within the (111) lattice plane with 120° between adjacent Mn atom spins, which is consistent with the existent experimental findings.[33]

Since Mn_3Pt films are in non-collinear antiferromagnetic order with rather weak net magnetization of around $5\,m\mu_B$ per Mn atom along the [001] directions,[29] the spin configurations of Mn_3Pt film can be manipulated and switched by applying appropriate out-of-plane magnetic fields. As depicted in Fig. 1(a), when sufficiently large 0.6 T magnetic field has been applied in the simulation, one of the three Mn spins turns to align with the external magnetic field, while the other two Mn spins rotate correspondingly to maintain a consistent 120° angle between neighboring Mn atoms. When the magnetic field has been swept back and forth, the net magnetization of Mn_3Pt films will form a standard magnetic hysteresis loop as it is shown in Fig. 1(b), akin to ferromagnetic film with perpendicular magnetic anisotropy (see Video S1 in the Supplemental Material[34]). Moreover, as plotted in Fig. 1(c), the coercive field H_c of Mn_3Pt film is found to be around several hundreds of Oe and proportional to its thickness. This observed increase in H_c can be attributed to the change of magnetic moment orientations of the three Mn atoms within the film, leading to increased Néel anisotropy energy reflected in the higher coercive field. A detailed explanation of this interplay between magnetic moments and H_c is provided in Note 1 of the Supplementary Material.[34] The dependence of coercive field $H_c$on Mn_3Pt film thickness makes it feasible to build a Mn_3Pt-based AFMTJ and to realize *parallel* and *antiparallel* aligned Néel configurations by preparing Mn_3Pt films with different thickness as left and right electrodes.

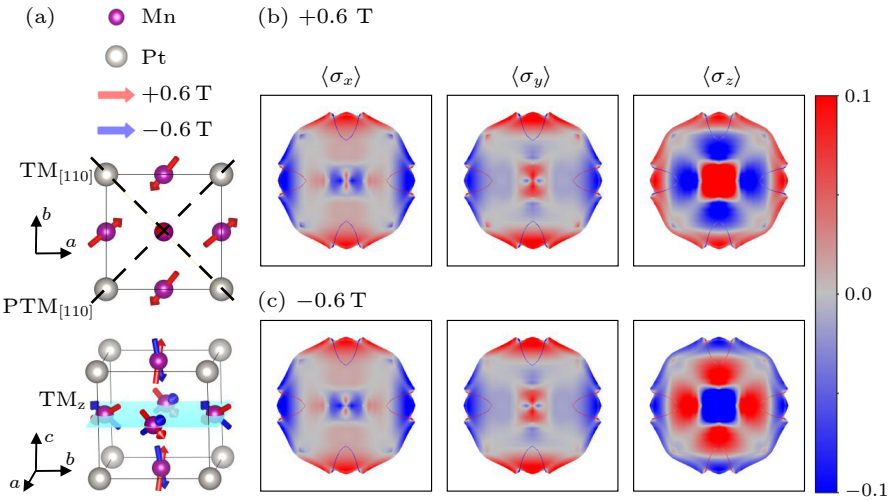

Fig. 2. (a) Atomic and spin structures of noncollinear AFM Mn_3Pt. The red and blue arrows indicate the orientations of spin moments on Mn atoms under positive and negative 0.6 T magnetic fields. The black dashed lines indicate two mirror planes $M_{[110]}$ and $PM_{[110]}$ perpendicular to ab plane and the cyan plane indicate the mirror plane M_z perpendicular to c axis. [(b), (c)] The top views for one of typical Fermi surface with projected spin expectation values of $\langle\sigma_x\rangle$, $\langle\sigma_y\rangle$, and $\langle\sigma_z\rangle$. The color bar alongside indicates the magnitude and sign of spin polarization.

According to the previous theory,[15] it is known that the appearance of momentum-dependent spin polarization in antiferromagnets, with no need for SOC, requires violation of both $TP\tau$ and $U\tau$ symmetries, where T is the time reversal symmetry, U is spinor symmetry, P is space inversion symmetry and τ is lattice translation. The noncollinear AFM atomic structures of bulk Mn_3Pt (MSG: $R\bar{3}m'$, $T_N = 365\,K$) are shown in Fig. 1(a), which indicate that Mn_3Pt has inversion symmetry but no time reversal symmetry, and its paramagnetic unit cells are the same as the AFM primitive cell. Therefore, Mn_3Pt violates both $TP\tau$ and $U\tau$ symmetries and should have spin-split band structures. To examine the electronic band structure of Mn_3Pt, we calculate its momentum-dependent spin polarization by taking the simulated spin configurations under +0.6T and −0.6T magnetic fields. Figure 2 shows the calculated spin expectation values of $\langle\sigma_x\rangle$, $\langle\sigma_y\rangle$, and $\langle\sigma_z\rangle$ projected on one of the six Fermi surfaces of Mn_3Pt. As demonstrated in Figs. 2(b) and 2(c), the distinctive characteristics of a typical spin-splitting noncollinear antiferromagnet are evident in Mn_3Pt, showcasing momentum-dependent spin polarization on its Fermi surface. Noteworthily, the z-component of spin polarization $\langle\sigma_z\rangle$ undergoes a sign reversal when the direction of the applied 0.6 T magnetic field is reversed, while the in-plane spin polarization $\langle\sigma_x\rangle$ and $\langle\sigma_y\rangle$ remain nearly unchanged.

The symmetry of spin polarization shown in Figs. 2(b) and 2(c) can be understood from the existing symmetry

operations of Mn_3Pt. As indicated in Fig. 2(a), there are three mirror reflection planes including two mirrors $M_{[110]}$, $PM_{[110]}$ perpendicular to ab planes, and one mirror M_z perpendicular to c axis. The three mirror reflections combined with time reversal lead to three symmetry operations $TM_{[110]}$, $PTM_{[110]}$ and TM_z. With those symmetry restrictions, the wave vector and the spin polarization of Bloch electron will be transformed as follows:

$$\begin{aligned} PTM_{[110]}:\ & (k_x,\, k_y,\, k_z) \to (-k_y,\, -k_x,\, k_z),\\ & (\sigma_x,\, \sigma_y,\, \sigma_z) \to (-\sigma_y,\, -\sigma_x,\, \sigma_z);\\ TM_{[110]}:\ & (k_x,\, k_y,\, k_z) \to (k_y,\, k_x,\, -k_z),\\ & (\sigma_x,\, \sigma_y,\, \sigma_z) \to (-\sigma_y,\, -\sigma_x,\, \sigma_z);\\ TM_z:\ & (k_x,\, k_y,\, k_z) \to (-k_x,\, -k_y,\, k_z),\\ & (\sigma_x,\, \sigma_y,\, \sigma_z) \to (\sigma_x,\, \sigma_y,\, -\sigma_z). \end{aligned}$$

The analysis reveals a two-fold symmetry for in-plane spin polarization $\langle\sigma_x\rangle$ and $\langle\sigma_y\rangle$, and a four-fold symmetry for $\langle\sigma_z\rangle$. Furthermore, it can be deduced that $\langle\sigma_z\rangle$ exhibits antisymmetry (sign change) respecting to spin configurations flipped by positive and negative 0.6 T magnetic fields, while the in-plane spin polarizations (σ_x, σ_y) remain unchanged. This symmetry analysis aligns with the calculated results depicted in Figs. 2(b) and 2(c).

Based on the spin-splitting Fermi surface discussed above, the noncollinear antiferromagnet Mn_3Pt can readily serve as electrodes in AFMTJs with structure of Mn_3Pt/barrier/Mn_3Pt, where the junction conductance will depend on the relative orientation of Néel vectors between the left and right Mn_3Pt electrodes. To elucidate the origin of TMR in Mn_3Pt-based AFMTJ and distinguish it from ferromagnetic MTJs, in Fig. 3 we illustrate three different kinds of tunnel junctions by using ferromagnets (FMs), conventional spin-degenerated antiferromagnets (C-AFMs), and spin-splitting antiferromagnets (SS-AFMs) as electrodes. In the context of ballistic transport, we make the assumption that the transverse wave vector $\boldsymbol{k}_{||} = (k_x,\, k_y)$ and the spin polarization of Bloch electrons remain conserved during the tunneling process. In ferromagnetic MTJs illustrated in Fig. 3(b), the alignment of magnetizations in the *parallel* alignment (P) results in matched spin channels between the fixed and the free layer, leading to higher transmission compared to the *antiparallel* alignment (AP).[35] This phenomenon gives rise to the TMR effect. However, in the case of C-AFMs in AFMTJs, as the two spin channels of C-AFMs are identical, the conductance remains the same for both P and AP configurations of the Néel vector. Consequently, one would not expect TMR effect in this scenario. However, in the case of AFMTJs employing SS-AFMs as electrodes like Mn_3Pt/barrier/Mn_3Pt AFMTJ, the electron transmission is governed by the alignment of momentum-dependent spin polarization at each $\boldsymbol{k}_{||}$ point between the free and fixed Mn_3Pt layers. As a result, the tunneling conductance in the AFMTJs is determined by the Néel vector alignments of the two electrodes, leading to a prominent TMR effect. It is worth noting that the origin of TMR in AFMTJ based on spin-splitting AFMs should be distinguished from that in ferromagnetic MTJs. In the latter case, a net magnetic moment and an exchange splitting band structure of the ferromagnet are imperative for producing the TMR effect. However, in spin-splitting AFM-based AFMTJs such as Mn_3Pt/barrier/Mn_3Pt, the presence of a net magnetic moment in the AFM electrode is not necessary.

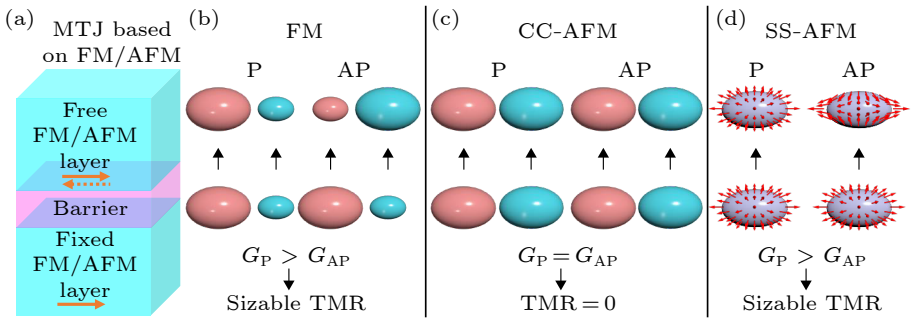

Fig. 3. (a) Schematic of tunnel junctions by using FM and AFM as electrodes. The orange arrows indicate the directions of magnetization for FM and Néel vector for AFM. (b)–(d) Schematic of TMR effect in tunnel junctions based on FM, spin-degenerated AFM and spin-splitting AFM. The pink (cyan) ellipsoids in (b) and (c) represent the Fermi surfaces for majority and minority spin channels, while the red arrows in (d) imply the vector direction of spin polarization on Fermi surface for spin-splitting AFMs.

Finally, we have constructed AFMTJs with the structure of Mn_3Pt/perovskite oxides/Mn_3Pt and performed first-principles calculations of the spin-dependent transport properties. In the selection of perovskites materials, we first select $PbTiO_3$ as the tunnel barrier due to its minimal lattice mismatch with Mn_3Pt. Specifically, the lattice constant of the cubic $PbTiO_3$ is 3.90 Å,[36] while the experimental in-plane lattice constant of Mn_3Pt thin film is 3.85 Å,[29] resulting in a small lattice mismatch of 1.3%. As depicted in Fig. 4(a), the structure of $Mn_3Pt/PbTiO_3/Mn_3Pt$ AFMTJ is illustrated, demonstrating the *parallel* and *antiparallel* spin configurations between the left and right electrodes. The energy favorable interface structure between Mn_3Pt and $PbTiO_3$ has been

investigated by calculating the formation energy demonstrated in Fig. S2 in the Supplementary Material.[34] Additionally, through first principles calculations, we find that the Fermi energy of the tunnel junction is located in the bottom of the conduction band of the potential barriers $PbTiO_3$, as shown in Fig. S3.[34]

The calculated conductance ratio between the *parallel* and *antiparallel* aligned magnetic configurations in $Mn_3Pt/PbTiO_3$ (9 MLs)/Mn_3Pt AFMTJ is found to be $G_P/G_{AP} \approx 9.6$, corresponding to a TMR of around 860% based on the conventional TMR definition $[TMR = (G_P/G_{AP}\text{-}1)\times 100\%]$[8] where the computation details are elaborated in Note 4 of the Supplemental Material.[34] Note that such a large TMR is eight times of that in previously studied $Mn_3Sn/1T\text{-}HfO_2/Mn_3Sn$ AFMTJ and even much larger than the TMR obtained in conventional $CoFe/AlO_x/CoFe$ ferromagnetic MTJs.[9,10] As listed in Table 1, the resistance–area products (RA) of the $Mn_3Pt/PbTiO_3/Mn_3Pt$ AFMTJ is relatively low, for *parallel* and *antiparallel* alignment cases are $1.079\,\Omega\cdot\mu m^2$ and $10.350\,\Omega\cdot\mu m^2$, respectively. Moreover, we have scanned the energy in the range of 1.0 eV below the Fermi energy of $Mn_3Pt/PbTiO_3/Mn_3Pt$ tunnel junction to explore the energy dependence of the TMR effect. The results illustrated in Fig. S4 in Supplemental Material[34] show robust and considerable TMR ratio when the energy is shifted deeper into the band gap of the insulator barriers.

Table 1. Calculated resistance–area product (RA) and TMR ratio of single-crystalline Mn_3Pt-based AFMTJs by using $PbTiO_3$, $SrTiO_3$ and MgO as tunnel barriers.

Tunnel barriers	RA-P ($\Omega\cdot\mu m^2$)	RA-AP ($\Omega\cdot\mu m^2$)	TMR (%)
$PbTiO_3$-9 MLs (1.63 nm)	1.079	10.350	859
$SrTiO_3$-9 MLs (1.60 nm)	0.357	1.224	243
MgO-9 MLs (1.85 nm)	2289.788	2361.652	3

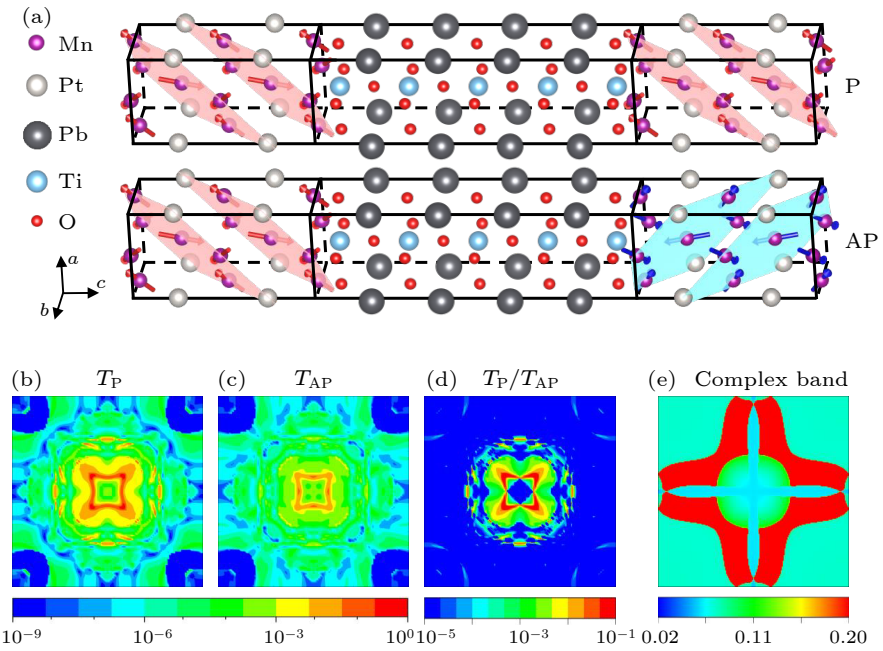

Fig. 4. (a) Schematic of the $Mn_3Pt/PbTiO_3/Mn_3Pt$ AFMTJ for the *parallel* (P) and *antiparallel* (AP) magnetic configurations. [(b), c)] The $\boldsymbol{k}_{||}$-resolved transmission $T(\boldsymbol{k}_{||})$ for P and AP states by using $PbTiO_3$ as tunnel barriers. (d) Transmission ratio T_P/T_{AP}. (e) The smallest imaginary part of complex band κ (in units of $2\pi/a$) at the middle of band gap of $PbTiO_3$ in the 2D Brillouin zone.

To further elucidate the origin of the remarkable TMR in $Mn_3Pt/PbTiO_3/Mn_3Pt$ AFMTJ, Figs. 4(b)–4(d) present the $\boldsymbol{k}_{||}$-resolved electron transmission $T(\boldsymbol{k}_{||})$ and the transmission ratio $T_P(\boldsymbol{k}_{||})/T_{AP}(\boldsymbol{k}_{||})$ in the 2D Brillouin zone for *parallel* and *antiparallel* spin configurations. It is revealed that the substantial transmission ratio, and consequently the TMR, can be primarily attributed to the $\boldsymbol{k}_{||}$ points away from Γ point [$\boldsymbol{k}_{||} = (0, 0)$]. In a tunnel junction, the electron tunneling probability is proportional to $\exp(-2\kappa d)$, where κ is the imaginary part of the complex band and d is the thickness of the tunnel barrier.[37] Figure 4(e) illustrates the smallest imaginary part of the complex band κ (representing the lowest decay rates of the evanescent states) for $PbTiO_3$. It demonstrates that κ is relatively low across a significant portion of the Brillouin zone, resulting in large transmission at the $\boldsymbol{k}_{||}$ points away

from the Γ point. This situation contrasts with the case of using MgO as a tunnel barrier, as we will discuss later, where the complex band κ can be found in Fig. S5.[34]

The mechanism of the TMR effect in this type of tunnel junctions lies in the specific MSG of the electrodes, rather than the influence of SOC itself. To assess the impact, we have compared the band structures of bulk Mn_3Pt with and without considering SOC effect. As shown in Fig. S6,[34] SOC exerts negligible influence on this type of Mn_3Pt-based tunnel junctions due to the minimal difference of the band structures at the Fermi energy, except for insignificant deviations at the Γ point.

Additionally, the substantial TMR effect may also be achieved by selecting other perovskite oxides as tunnel barriers with complex band structures similar to $PbTiO_3$. To confirm this point, we perform transport calculations in Mn_3Pt-based AFMTJs by using $SrTiO_3$ as barrier. As outlined in Table 1, the conductance ratio G_P/G_{AP} in $Mn_3Pt/SrTiO_3$(9 MLs)/Mn_3Pt AFMTJ is found to be 3.4, corresponding to the TMR ratio of about 240%, which can also be found in our previous report.[38] In contrast, the TMR in Mn_3Pt/MgO (9 MLs)/Mn_3Pt AFMTJ is only 3%. This result can also be quantitatively understood from the complex band distribution in 2D Brillouin zone shown in Fig. S5 and the transmission of AFMTJs-based on Mn_3Pt with MgO as barriers.[38] The transmission ratio T_P/T_{AP} clearly indicates that the electronic states near the Γ point do not have significant contribution to the TMR effect, whereas the states away from Γ point play a crucial role. This suggests that to achieve a substantial TMR in AFMTJs with Mn_3Pt electrodes, the transmission should not be dominated by states near Γ point. Since MgO has much lower decay rates circling around Γ point, the electron transmission is dominated by Bloch states near the Γ point, resulting in relatively low TMR. In addition to $PbTiO_3$ and $SrTiO_3$, as depicted in Fig. S5,[34] we also calculate the complex bands for other perovskite oxides, which also have small lattice mismatch with Mn_3Pt. These oxides should be suitable for achieving similarly large TMR effect as $PbTiO_3$ and $SrTiO_3$. Please note that the origin of the large TMR effect in Mn_3Pt-based AFMTJs is fundamentally different from that in Fe/MgO/Fe MTJs, where significant TMR arises from the spin-polarized Δ_1 bands of *bcc*-Fe and spin-filter effect of MgO at Γ point.[11]

In summary, by performing atomistic spin dynamic simulations, we theoretically reveal the magnetic switching process of noncollinear AFM Mn_3Pt thin film and show that the coercive field of Mn_3Pt films increases with thickness. We showcase the feasibility of constructing AFMTJs by preparing Mn_3Pt films with varying thickness as electrodes and investigating the momentum-dependent spin polarization under positive and negative 0.6 T magnetic fields. In AFMTJs based on Mn_3Pt with single crystal perovskite oxides as tunneling barriers, substantial TMR effects exceeding 800% are observed. Our work not only presents viable materials and interface structures for achieving large TMR ratios in AFMTJs, but also offers guidance for exploring the next-generation high-speed, high-density antiferromagnetic memory devices.

Acknowledgement. J.Z. was supported by the National Natural Science Foundation of China (Grant Nos. T2394475, T2394470, and 12174129).

References

[1] Jungwirth T, Sinova J, Manchon A, Marti X, Wunderlich J, and Felser C 2018 *Nat. Phys.* **14** 200
[2] Baltz V, Manchon A, Tsoi M, Moriyama T, Ono T, and Tserkovnyak Y 2018 *Rev. Mod. Phys.* **90** 015005
[3] Wadley P, Howells B, Železny J, Andrews C, Hills V, Campion R P, Novák V, Olejník K, Maccherozzi F, Dhesi S S, Martin S Y, Wagner T, Wunderlich J, Freimuth F, Mokrousov Y, Kuneš J, Chauhan J S, Grzybowski M J, Rushforth A W, Edmonds K W, Gallagher B L, and Jungwirth T 2016 *Science* **351** 587
[4] Bodnar S Y, Šmejkal L, Turek I, Jungwirth T, Gomonay O, Sinova J, Sapozhnik A A, Elmers H J, Kläui M, and Jourdan M 2018 *Nat. Commun.* **9** 348
[5] Hoogeboom G R, Aqeel A, Kuschel T, Palstra T T M, and van Wees B J 2017 *Appl. Phys. Lett.* **111** 052409
[6] Fischer J, Gomonay O, Schlitz R, Ganzhorn K, Vlietstra N, Althammer M, Huebl H, Opel M, Gross R, Goennenwein S T B, and Geprägs S 2018 *Phys. Rev. B* **97** 014417
[7] Chiang C C, Huang S Y, Qu D, Wu P H, and Chien C L 2019 *Phys. Rev. Lett.* **123** 227203
[8] Tsymbal E Y, Mryasov O N, and LeClair P R 2003 *J. Phys.: Condens. Matter* **15** R109
[9] Higo T and Nakatsuji S 1995 *J. Magn. Magn. Mater.* **139** L231
[10] Moodera J S, Kinder L R, Wong T M, and Meservey R 1995 *Phys. Rev. Lett.* **74** 3273
[11] Butler W H, Zhang X G, Schulthess T C, and MacLaren J M 2001 *Phys. Rev. B* **63** 054416
[12] Yuasa S, Nagahama T, Fukushima A, Suzuki Y, and Ando K 2004 *Nat. Mater.* **3** 868
[13] Ozatay O, Mather P G, Thiele J U, Hauet T, and Braganca P M 2011 *Comprehensive Nanosci. Nanotechnol.* **4** 561
[14] Wadley P, Hills V, Shahedkhah M R, Edmonds K W, Campion R P, Novák V, Ouladdiaf B, Khalyavin D, Langridge S, Saidl V, Nemec P, Rushforth A W, Gallagher B L, Dhesi S S, Maccherozzi F, Železny J, and Jungwirth T 2015 *Sci. Rep.* **5** 17079
[15] Yuan L D, Wang Z, Luo J W, and Zunger A 2021 *Phys. Rev. Mater.* **5** 014409
[16] Hayami S, Yanagi Y, and Kusunose H 2019 *J. Phys. Soc. Jpn.* **88** 123702
[17] Šmejkal L, Sinova J, and Jungwirth T 2022 *Phys. Rev. X* **12** 011028
[18] Shao D F, Zhang S H, Li M, Eom C-B, and Tsymbal E Y 2021 *Nat. Commun.* **12** 7061
[19] Šmejkal L, González-Hernández R, Jungwirth T, and Sinova J 2020 *Sci. Adv.* **6** eaaz8809
[20] Ahn K-H, Hariki A, Lee K-W, and Kuneš J 2019 *Phys. Rev. B* **99** 184432
[21] Berlijn T, Snijders P C, Delaire O, Zhou H-D, Maier T A, Cao H B, Chi S X, Matsuda M, Wang Y, Koehler M R, Kent P R C, and Weitering H H 2017 *Phys. Rev. Lett.* **118** 77201
[22] Chen H, Niu Q, and MacDonald A H 2014 *Phys. Rev. Lett.* **112** 017205
[23] Kübler J and Felser Cr 2014 *Europhys. Lett.* **108** 67001
[24] Zhang Y, Sun Y, Yang H, Železny J, Parkin S P P, Felser C, and Yan B 2017 *Phys. Rev. B* **95** 075128
[25] Zhang Y, Železný J, Sun Y, Brink J V D, and Yan B 2018 *New J. Phys.* **20** 073028

[26] Kimata M, Chen H, Kondou K, Sugimoto S, Muduli P K, Ikhlas M, Omori Y, Tomita T, MacDonald A H, Nakatsuji S, and Otani Y 2019 *Nature* **565** 627
[27] Dong J T, Li X L, Gurung G, Zhu M, Zhang P N, Zheng F X, Tsymbal E Y, and Zhang J 2022 *Phys. Rev. Lett.* **128** 197201
[28] Brown P J, Nunez V, Tasset F, Forsyth J B, and Radhakrishna P 1990 *J. Phys.: Condens. Matter* **2** 9409
[29] Liu Z Q, Chen H, Wang J M, Liu J H, Wang K, Feng Z X, Yan H, Wang X R, Jiang C B, Coey J M D, and MacDonald A H 2018 *Nat. Electron.* **1** 172
[30] Mukherjee J, Suraj T S, Basumatary H, Sethupathi K, and Raman K V 2021 *Phys. Rev. Mater.* **5** 014201
[31] Evans R F L, Fan W J, Chureemart P, Ostler T A, Ellis M O A, and Chantrell R W 2014 *J. Phys.: Condens. Matter* **26** 103202
[32] Jenkins S, Fan W J, Gaina R, Chantrell R W, Klemmer T, and Evans R F L 2020 *Phys. Rev. B* **102** 140404
[33] Krén E, Kádár G, Pál L, Sólyom J, Szabó P, and Tarnóczi T 1968 *Phys. Rev.* **171** 574
[34] See the Supplemental Material for details of Mn_3Pt switching dynamics, magnetic anisotropy energy as a function of film thickness, interface formation energy, layer-resolved density of states, and TMR as a function of energy in $Mn_3Pt/PbTiO_3/Mn_3Pt$ tunnel junction, and the computational details on self-consistent, transmission of magnetic tunnel junction and lowest decay rates of the evanescent states for other perovskites, band structure of bulk Mn_3Pt.
[35] Li X L, Lü J T, Zhang J, You L, Su Y R, and Tsymbal E Y 2019 *Nano Lett.* **19** 5133
[36] Nelmes R J and Kuhs W F 1985 *Solid State Commun.* **54** 721
[37] Velev J P, Belashchenko K D, Stewart D A, van Schilfgaarde M, Jaswal S S, and Tsymbal E Y 2005 *Phys. Rev. Lett.* **95** 216601
[38] Qin P, Yan H, Wang X, Chen H, Meng Z, Dong J, Zhu M, Cai J, Feng Z, Zhou X, Liu L, Zhang T, Zeng Z, Zhang J, Jiang C, and Liu Z 2023 *Nature* **613** 485